Simulation of high-velocity impact onto a liquid filled container

Shashanka Subrahmanya, Georg A. Heilig, Michael May

Fraunhofer Institute for High-Speed Dynamics, Ernst-Mach-Institut, EMI

Freiburg im Breisgau, 79104, Germany

Abstract

At EMI, a series of experiments has been conducted to investigate the deformation and failure of tanks filled with tap water when subjected to high-speed impact loading. The present experiments investigate the Hydrodynamic RAM (HRAM) effect, a phenomenon of high importance for aircraft safety. Throughout their operational lifespan, aircraft may encounter various foreign object impact scenarios, such as birds or drones striking the leading edges of their wings. In military contexts, impacts from metallic warhead splitters can also induce the undesirable HRAM effect. In the laboratory, HRAM is simulated through generic high-speed impacts of solid projectiles on cuboid tanks filled with tap water as a surrogate for aviation fuel, which possesses mechanical properties comparable to those of conventional fuels while reducing the risk of fire and other hazard. HRAM is a complex phenomenon characterized by the simultaneous occurrence of multiple physical processes, such as impact induced stresses, initiation of shock waves, forming of cavities, which subsequently fills with atmospheric air that enters the tank through the penetration orifice. The experiments are modeled using two hydrocodes, Ansys LS-DYNA and Ansys AUTODYN-3D, respectively, in a fully coupled fluid-structure interaction mode. This paper presents a comparison between the experimental and numerical results for a scenario with an impact velocity V_0 = 645 m/s. The primary focus is on the velocity decay of the cylindrical, flat-nosed aluminum projectile (L/D = 2) in water, as well as the growth and decay of the induced cavity.

1 Introduction

During their operational lifespan, aircraft may encounter various foreign object impact scenarios, including birds [1] or drones [2], striking the leading edge of the wing, where fuel tanks are typically integrated. The impact of a foreign object on the fuel tank can result in the undesirable Hydrodynamic RAM (HRAM) effect [3]. This effect is a complex phenomenon characterized by several physical processes occurring simultaneously.

In laboratory settings, HRAM is simulated through high-speed impacts on tanks filled with tap water using solid projectiles. This method is advantageous as water shares similar physical properties with aviation fuel while eliminating fire hazards. Heilig and May [4] provide a comprehensive overview of HRAM-related research over the past 125 years, highlighting the evolution of experimental, numerical, and analytical approaches.

Varas et al. [5] were among the first to describe four subsequent HRAM stages, which depend on the material properties of the components involved, the kinetic energy of the projectile, and the structural configuration of the tank. The severity of each stage varies due to the dynamic fluid phenomena induced within the static fluid. The stages have been referred to by different names in the literature, and additional stages have been introduced based on specific test conditions. Chen et al. [6] expanded this classification to five phases:

(a) **Penetration Phase:** In this initial phase, the projectile transfers its kinetic energy to the tank, effectively "punching" an orifice into the front plate.

(b) **Shock Phase:** As the projectile penetrates the liquid, it generates several hemispherical shock waves that propagate towards the tank's confinement.

(c) **Drag-Cavity Phase:** During this phase, the projectile's energy is dissipated due to the drag it experiences while moving through the liquid, resulting in the formation of a conical cavity filled with air

and vapor. Although the pressure values in this stage are not as high as those in the shock phase, it has a longer duration.

(d) **Exit Phase:** If the projectile's energy has not been fully dissipated during the first three phases, it may punch an orifice into the back plate, potentially leading to cracking of the plate.

(e) **Cavity Oscillation Phase:** Regardless of whether the projectile has created an orifice in the back plate or has rebounded due to insufficient kinetic energy, the cavity undergoes a repetitive process of contraction and expansion after reaching its maximum volume. This oscillation continues until the cavity ultimately collapses, breaking into small bubbles that no longer expand.

During this event, the liquid in the container may spurt from the penetration orifices. This liquid spurt is disrupted by strong aerodynamic disturbances, leading to rapid atomization into small droplets. As illustrated in Fig.1:, a notable characteristic of the HRAM effect is the dynamic evolution of the cavity, which includes phases of expansion, contraction, collapse, and subsequent oscillations.

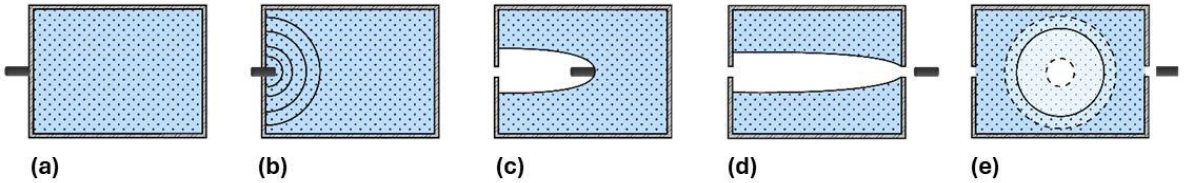

Fig.1: Sketch of five HRAM phases.

2 Experimental setup

The experimental setup, illustrated in Fig. 2, is as follows: a cylindrical, flat-nosed aluminum projectile is accelerated towards a cuboidal tank completely filled with tap water. The tank has inner dimensions of 400 mm x 500 mm x 410 mm, resulting in a volume of 82 liters. Although a comprehensive series of experiments was conducted at various impact velocities, this paper focuses on a specific experiment with an impact velocity of V_0 = 645m/s.

The tank is constructed with 3 mm thick front and rear aluminum plates (AW2017A, ρ = 2.785 g/cm^3), and four transparent lateral polycarbonate plates (thickness = 10 mm, ρ = 1.20 g/cm^3) to enable high-speed video recording, as shown in Fig. 2. The aluminum projectile has a length of 32 mm and a diameter of 16 mm (L/D = 2), with a mass of 18.46 g (ρ = 2.804 g/cm^3).

The acceleration of the cylindrical aluminum projectile is achieved using a single-stage gas gun, which can be operated with either compressed air or powder. The facility consists of (1) a high-pressure chamber, (2) an accelerator tube (gun barrel) with an inner diameter of 18 mm and a length of 2 m, and (3) an instrumented impact chamber equipped with windows for high-speed video recording, which contains (4) the water-filled tank.

For projectile acceleration, no sabot is utilized. Instead, two polycarbonate-guide rings are employed, featuring an outer diameter that matches the inner diameter of the gun barrel and an inner diameter slightly larger than that of the projectile. To accommodate the two 18 mm diameter guide rings within the gas gun, grooves were machined into the projectile. The projectile has a diameter of 14 mm for the first 6 mm from the rear, followed by a diameter of 16 mm for the next 6 mm, and then a groove leading to a diameter of 14 mm for the subsequent 4 mm and back to a diameter of 16 mm for the rest of its total length. The aluminum body of the projectile weighs 16.70 g. Including the two guide rings (with masses of 0.45 g and 1.15 g) and the adhesive bond (0.16 g), the total weight of the projectile increases to 18.46 g.

Fig.2: illustrates a sketch of the setup, where the cylindrical body (diameter 16 mm, 18.35 mm including the guide rings) is shown in black and the guide rings are depicted in blue.

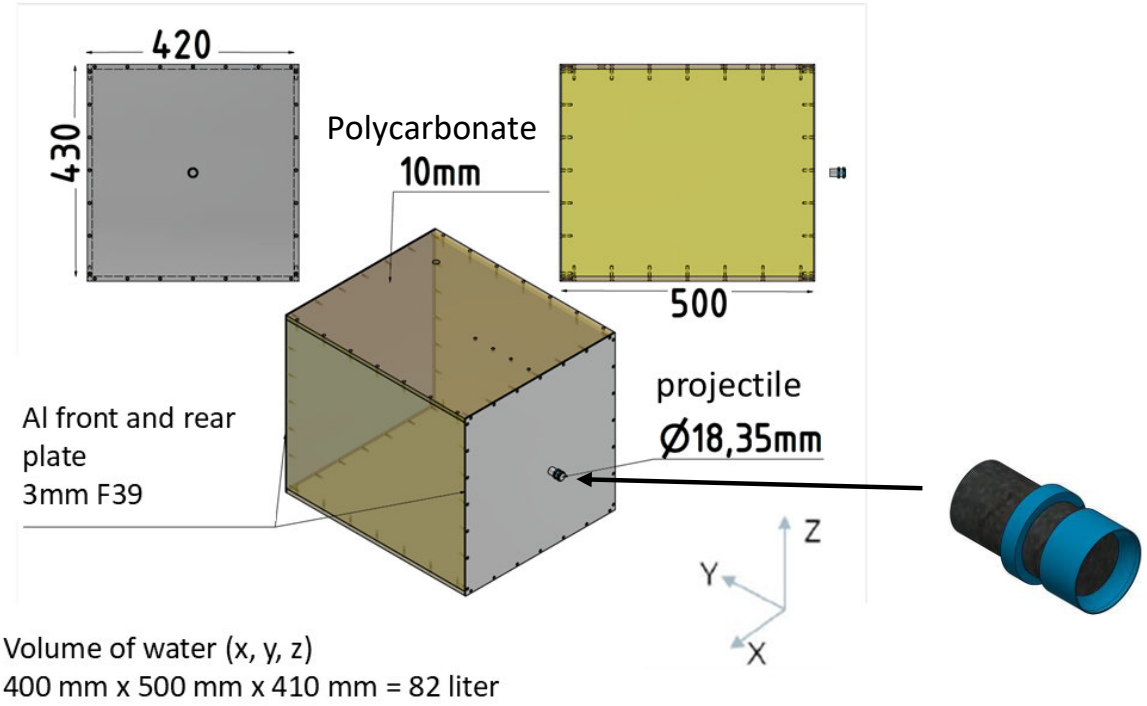

Fig.2: Sketch of the tank with axis convention (left) and sketch of the aluminum projectile with guiding rings (right). The aluminum front and rear plate of the tank are shown in grey, the four lateral polycarbonate plates are in yellow, the aluminum projectile is black, the shot direction is the y-direction.

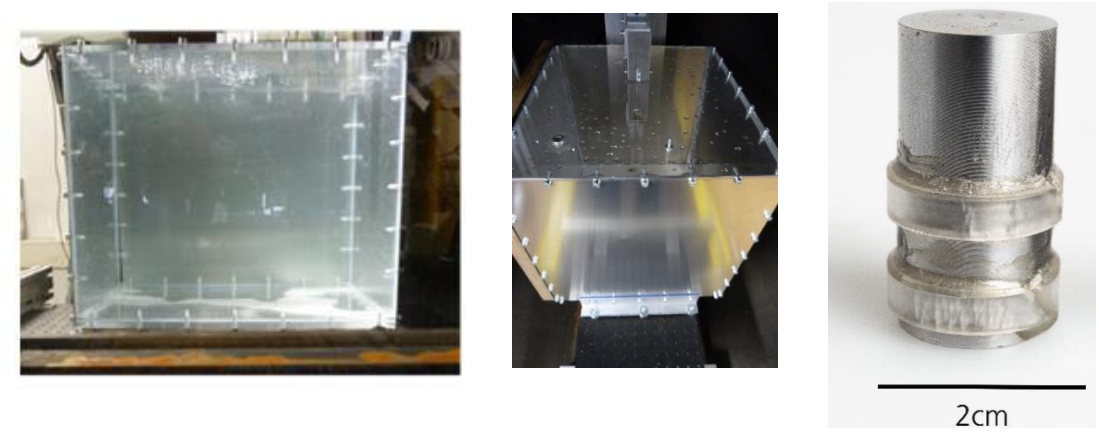

Fig.3: Photographs of the water filled tank and of the cylindrical, flat-nosed aluminum projectile before impact.

Fig.4: presents two high-speed images from the experiment conducted at V_0 = 645m/s at two different time intervals. The images illustrate the projectile's movement through the water and the growth of the air-filled cavity that forms behind it, which is caused by pressure drag. In this case, no exit phase is observed; instead, the projectile rebounds off the aluminum rear plate and remains inside the tank.

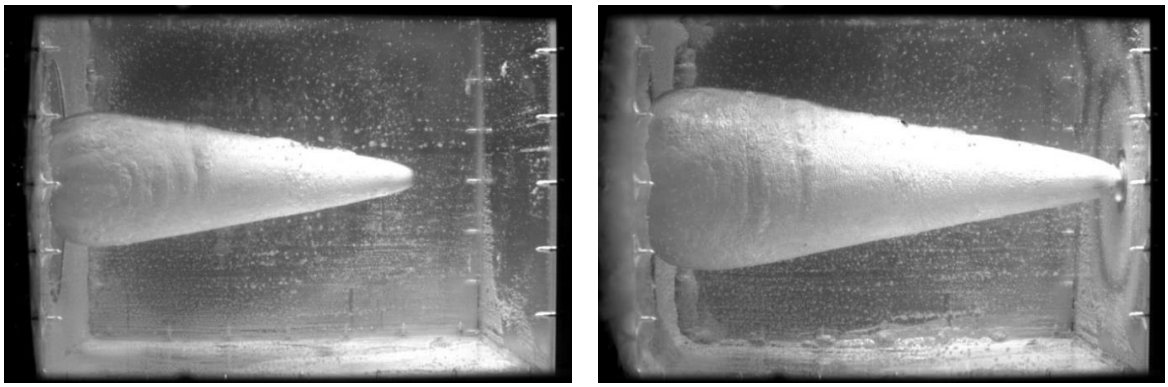

Fig.4: Experimental images at t = 1,600 µs and 3,000 µs.

3 Numerical setup

To simulate the HRAM effect, a simulation model is established using the LS-DYNA Structured Arbitrary Lagrangian Eulerian (S-ALE) methodology and compared with a model in AUTODYN-3D utilizing full Euler-Lagrange coupling (Multi-Material Godunov processor). Given that the projectile experiences minimal to no damage in the experiment and that the focus of this study does not lie on projectile damage, the projectile is modelled as a rigid body to reduce computational costs.

The S-ALE solver which was first introduced to LS-DYNA in 2015, is similar to ALE but dedicated to solving the subset of ALE problems where a structured mesh comes into picture. The S-ALE solver runs faster, offers a hassle-free three step model setup and is better optimized against leakage compared to the older ALE method. Many settings and decisions that should have previously been taken by the user in the ALE method are eliminated and automatically calculated in the S-ALE solver making it much more user-friendly. The user must tune only one parameter called the Penalty Factor (PFAC) defined in the **`*ALE_STRUCTURED_FSI`** card which can be used to vary the penalty stiffness to achieve the desired fluid-structure coupling [7].

Initially in LS-DYNA S-ALE, an attempt was made to set up the simulation using similar material models and formulations as those in the previously published AUTODYN-3D model by Heilig and May [8]. However, due to discrepancies in the quality of results between LS-DYNA and the AUTODYN-3D models—primarily including parameters from the AUTODYN-3D material library—the simulation was reconfigured in LS-DYNA using air and water models from Varas et al. [5].

The parameters for the structural components are defined similarly in both hydrocodes. However, in the comparison, shell elements with an edge size of 2 mm and theoretical thicknesses of 3 mm for the aluminum plates and 10 mm for polycarbonate plates are employed to discretize the tank in LS-DYNA, while solid elements with an edge size of 1.5 mm are utilized in AUTODYN-3D because there was a problem of leakage in AUTODYN-3D with shell elements. For clarity, the modelling approaches are summarized in Table 1:.

Table 1: Numerical setup. In AUTODYN-3D, the Euler region for air is geometrically smaller.

	LS-DYNA **Mesh size: Structures = 2 mm, Fluids 1.5 mm**	**AUTODYN-3D** **Mesh size: Structures = 1.5 mm, Fluids 1.45 mm**
Tank	305,350 shell elements (4 node)	1.22 million solid elements (8 node)
Projectile	8 node solids (rigid)	8 node solids (rigid)
Water and Air	39 million Euler elements	35 million Euler elements

In LS-DYNA, the aluminium plates were modelled using the commonly employed **`*MAT_024`** **`/*MAT_PIECEWISE_LINEAR_PLASTICITY`** card, which allows for the inclusion of the stress-strain curve to effectively represent the plastic behaviour of the material. The material parameters for

aluminium used in the simulations, along with the stress-strain curve obtained from tensile tests conducted on aluminium AW2017A at Fraunhofer EMI, are presented in Table 2: and **Error! Reference source not found.**, respectively.

The polycarbonate plates were modelled using the ***MAT_081/*MAT_PLASTICITY_WITH_DAMAGE** card, with the corresponding parameters detailed in 0. The contact between the projectile and the plates in the shell element model was defined using the ***CONTACT AUTOMATIC SURFACE TO SURFACE** card, with the **SOFT** parameter set to 1.

Table 2: Material parameters for aluminum plates in the tank [9].

Mass Density [g/mm³]	Young's Modulus [MPa]	Poisson's Ratio	Eff. Pl. Strain to Failure
2.8e-3	7000	0.33	0.05

*Table 3: Stress-strain curve values defined in aluminum *MAT_PIECEWISE_LINEAR_PLASTICITY material model obtained from tensile tests conducted on aluminum AW2017A at Fraunhofer EMI.*

True Strain [-]	True Stress [MPa]
0.00	250
0.02	343
0.04	385
0.06	417
0.08	442
0.10	462
0.12	477
0.14	491
0.16	501
0.18	509
0.20	516
0.22	523
0.24	529
0.26	534
0.28	538
0.30	542

Table 4: Material parameters for polycarbonate [10], [11].

Mass Density [g/mm³]	Young's Modulus [MPa]	Poisson's Ratio [-]	Yield Strength [MPa]	Eff. Pl. Strain to Failure [-]
1.19e-3	1800	0.43	143	0.4

The aluminum projectile was defined as a rigid cylinder with length 32 mm and diameter 16 mm using the ***MAT_020/*MAT_RIGID** card on LS-DYNA. This leads to a mass of 18.015 g. The material parameters for the projectile can be found in Table 5:.

*Table 5: Material parameters for aluminum projectile used in *MAT_RIGID card [9].*

Mass Density [g/mm³]	Young's Modulus [MPa]	Poisson's Ratio
2.8e-3	7000	0.33

The ***MAT_009/*MAT_NULL** material cards were utilized to define both air and water in the simulations. The equation of state for air was specified using the ***EOS_LINEAR_POLYNOMIAL** card, while the equation of state for water was defined using the ***EOS_GRUNEISEN** card. The material parameters for air and water are presented in Table 6: and Table 7:, respectively. The theoretical background for these cards in LS-DYNA can be found in [12].

*Table 6: Material parameters for air used in *MAT_NULL and *EOS_LINEAR_POLYNOMIAL cards [5].*

Mass Density, ρ_0 [g/mm³]	Dyn. Viscosity, v_d [MPa.ms]	C4 [-]	C5 [-]	Ini. Int. Energy / ref. Vol., E_0 [mJ/mm³]
1.22e-6	1.77e-8	0.4	0.4	0.253

*Table 7: Material parameters for water used in *MAT_NULL and *EOS_GRUNEISEN cards [5].*

Mass Density, ρ_0 [g/mm³]	Dyn. Viscosity v_d [MPa.ms]	Elast. Bulk wave velocity C [m/s]	Slope of v_s vs. v_p graph S [-]	Grueneisen γ_0 [-]	1st order vol. correction coeff. a [-]
1e-3	0.89e-6	1448	1.979	0.11	3.0

An Euler mesh size of 1.5 mm was selected, as the coupling behavior became unsatisfactory for sizes smaller than 1.5 mm when the Lagrange mesh size was fixed at 2 mm. For smaller mesh sizes, the S-ALE coupling resulted in insufficient deceleration of the projectile, causing it to penetrate the end plate, which did not occur in the experimental setup.

Regarding the simulation settings in S-ALE, a PFAC value of 0.01 provided the best coupling between the tank composed of shell elements, the rigid solid projectile, and the fluids, yielding acceptable results. The simulation, conducted on 32 processors MPP (Massively Parallel Processing), ran stably for 15,500 µs over a duration of 70.5 hours, successfully capturing the entire cavitation phase.

In the study of other velocity cases, which are outside the scope of this paper, a tank model with solid elements was also tested in LS-DYNA S-ALE. In this case, the coupling behavior was unrealistic with a PFAC value of 0.01. Starting from a PFAC value of 0.07, the model exhibited realistic behavior and demonstrated good coupling between the tank composed of solid elements, the rigid solid projectile, and the fluids. Among the PFAC values of 0.07, 0.08, and 0.09, the value of 0.07 yielded the best results. This indicates that a single PFAC value cannot be generalized for both solid and shell element models; instead, an optimal PFAC value must be determined for each specific case.

Fig.5: presents images from the LS-DYNA S-ALE simulation using shell elements at various time points, along with perspective views of color graded pressure plots. The LS-DYNA S-ALE methodology effectively recreates the HRAM effect qualitatively well up to the cavity oscillation phase. The projectile (depicted in golden yellow) enters the tank from the left at an initial velocity of V_0 = 645 m/s. The two cavity plots at the top of the figure show a well-defined cavity forming behind the moving projectile, which is filled with air from outside the tank. The projectile decelerates due to pressure drag while penetrating the front plate or interacting with the surrounding water. The cavity plots in the middle of the figure depict the rebounding of the projectile after impacting the end plate and the oscillation of the cavity, closely resembling the actual phenomenon. The perspective views of the pressure contours at the bottom of the figure visualize the motion of the shock wave generated upon the projectile's impact with both the aluminum front plate and the end plate.

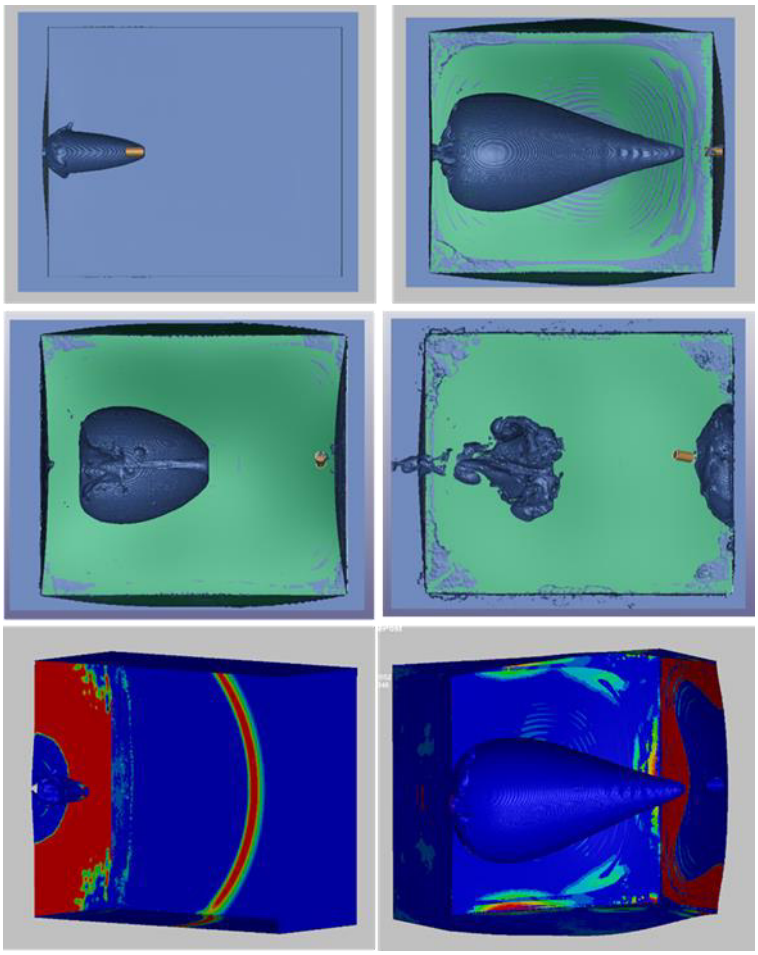

Fig.5: LS-DYNA S-ALE with shell element tank: Top-left: Cavity at t = 500 µs; Top-right: Cavity at t = 5,450 µs; Middle-left: Cavity at t = 10,000 µs; Middle-right: Cavity at t = 15,500 µs; Bottom-left: Perspective view of color graded pressure plot at t = 250 µs, Bottom-right: Perspective view of color graded pressure plot at t = 5,450 µs (blue: p = 0.9 bar, red: p = 13 bar)

Regarding the specifics of the AUTODYN-3D model, a Fluid-Structure Interaction (FSI) approach with full Euler-Lagrange coupling in the multi-material Godunov processor is employed. Fig.6: illustrates the numerical model and the pressure contours in water at two time points following the impact of the projectile on the front plate (shown in orange). Since the overall Euler discretization is finer than the Lagrange discretization (as detailed in Table 1:), the Euler-Lagrange contact algorithm functions effectively. In scenarios where the Euler discretization (for fluids) is coarser than the Lagrange discretization (for structures), small amounts of water may flow through regions where the plates remain undamaged by the impact process, as noted in [8].

The projectile (depicted in light blue) enters the tank from the left at an initial velocity of V_0 = 645 m/s. The two pressure contour plots at times after impact, t = 1,600 µs and t = 3,000 µs respectively, reveal a well-defined cavity forming behind the moving cylinder, filled with ambient air from outside the tank; note that the air is not displayed, either inside or outside the tank.

Due to the simultaneous presence of water (EOS: Mie-Gruneisen), air (EOS: ideal gas), and "void" in the Euler cells, the CFL time step Δt decreases to a very small value of 8.54e-10 s at time t = 6,861 µs, causing the computation to halt. For a simulation of this magnitude, AUTODYN-3D requires approximately 10 weeks to complete a simulation time of 10,000 µs in serial mode. A speedup could be attained using parallel computing; however, this approach was not utilized in the present study.

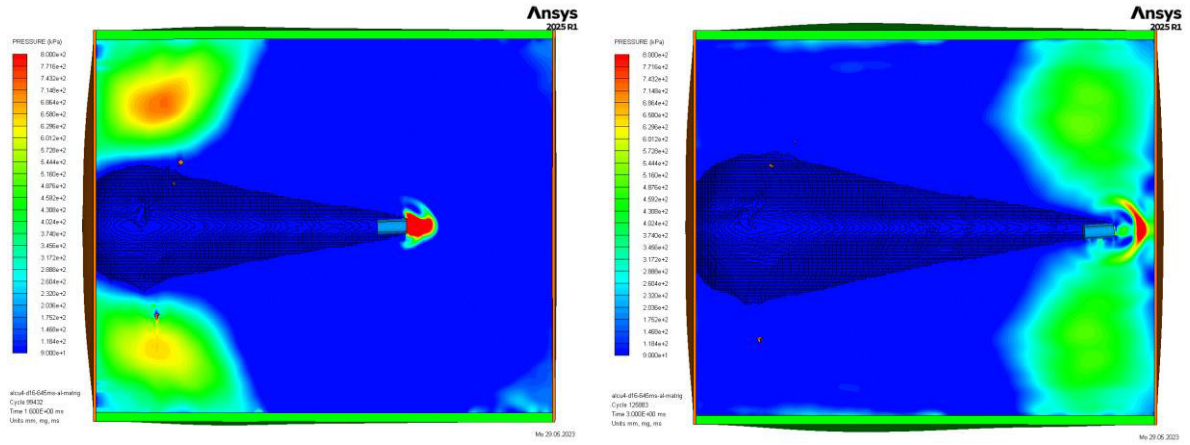

Fig.6: AUTODYN-3D numerical set-up and computed pressure contours (blue: p = 0.9 bar, red: p = 8.0 bar) at time t = 1,600 µs and t = 3,000 µs after impact. The ambient air which surrounds the tank and fills the cavity is not plotted.

To measure the cavity diameters in the LS-DYNA and AUTODYN-3D simulations, eight fixed locations were defined along the shot axis behind the front plate (y = 20 mm up to y = 160 mm in steps of 20 mm) since the maximum occurs before y = 160 mm. The diameters at these locations were recorded at regular time intervals and finally the maximum cavity diameter at each time interval was calculated.

Fig.7: illustrates the evolution of the air-filled cavity (depicted in magenta) at four different time points for the AUTODYN-3D simulation. The water inside the tank is not shown in order to facilitate the measurement of the cavity diameter. The projectile impacts the rear plate at approximately t = 4000 µs, rebounding without creating a hole or penetrating the plate. For t > 5200 µs, the cavity loses contact with the projectile, which is now tumbling with approximately zero velocity in front of the rear plate. Up to t = 6,800 µs, the cavity shrinks in the y-direction while maintaining its diameter in the z-direction. In the third and fourth plots, it is evident that the cylinder rebounds from the rear plate without penetrating it.

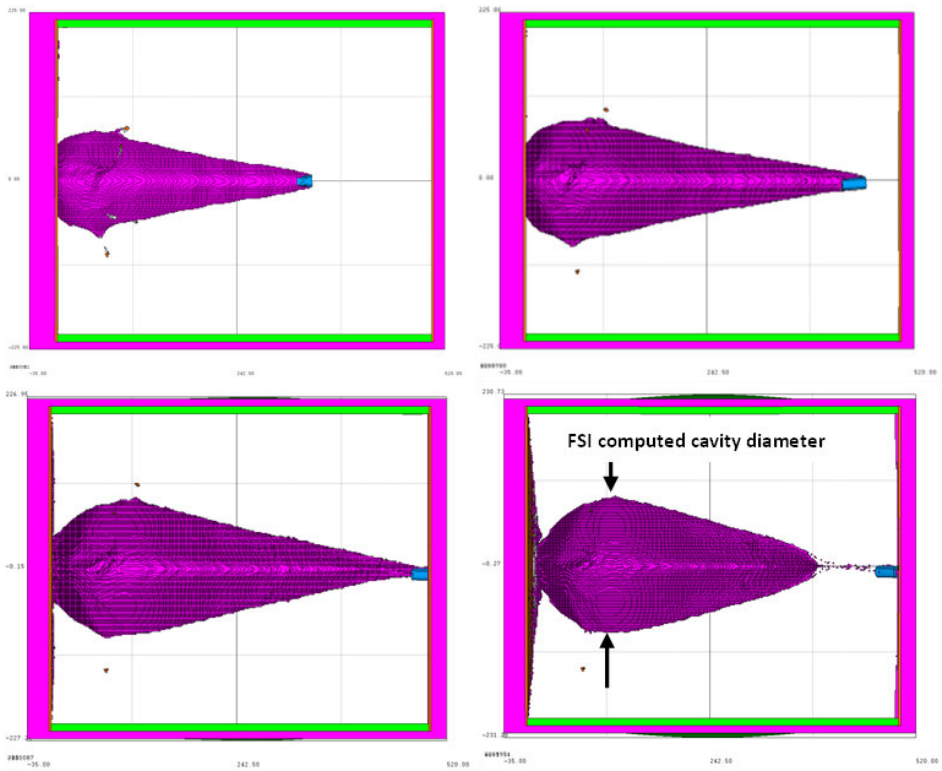

Fig.7: Evolution of the air-filled cavity (magenta) in AUTODYN-3D at times t = 1,600 µs, 3,000 µs, 5,000 µs, and 6,800 µs (from left to right) after impact in front view. The cavity surrounding water inside the tank is not plotted.

4 Analytical approach

In addition to the simulations and the experimental results, an analytical approach based on the works of Guo et al. [13] and Disimile & Toy [14] is presented. The kinetic energy of the projectile, given by $\frac{1}{2} m\, V_0^2$, is equal to the sum of the remaining kinetic energy of the projectile and the plug (a piece of the front plate displaced by the projectile to create a hole) after the projectile's impact with the front plate, as well as the energy transformed during the formation of the plug and the kinetic energy of the water being "pushed" inside the tank. According to [14], the energy balance can be expressed as follows:

$$\frac{1}{2} m\, V_0^2 = \left(m + \rho_f\, A_p\, t_f\right) \frac{V_{r0}^2}{2} + G\, L\, {t_f}^2 + \frac{1}{2} \rho_w\, V_{r0}^2\, A_p\, \left(D + t_f\right). \qquad (1)$$

Here, m and D, represent the mass and diameter of the projectile, respectively. The cross-sectional area of the projectile is given by $A_p = \frac{1}{4} \pi\, D^2$. The densities of the front plate material and water are denoted as ρ_f and ρ_w, respectively. The shear yield strength of the front plate is represented by G. L is the peripheral length of the penetration hole, and t_f is the thickness of the front plate.

The equation above provides an expression for the velocity V_{r0} of the projectile after it has penetrated the front plate and begins to enter the water. In equation (1), V_{r0} depends solely on the impact velocity and is not a function of time. If the front plate has a hole at the impact point, the thickness of the plate is effectively zero, and the reduced velocity can be expressed as follows:

$$V_{r0}^2 = \frac{m V_0^2}{\left(m + \rho_w A_p D\right)}.$$

Following [13] (section 3.2 *Projectile dynamics*)**,** the projectile's equation of motion is:

$$m\, \frac{\mathrm{d}V_r}{\mathrm{d}t} = -\frac{1}{2} \rho_w\, C_d\, V_r^2 \quad \text{with} \quad C_d = C_0 \left(1 + \sigma_0\, \frac{V_{r0}^2}{V_r^2}\right) \quad \text{and} \quad \sigma_0 = \frac{C_a\, \rho_a}{\rho_W}$$

It is valid along the shot axis y = 0. Possible tumbling and drifting of the projectile travelling through the water is not included; V_r is a function of time. $\rho_a$is the air density. C_0 ≈ 0.82 is the dimensionless drag coefficient for a long cylinder and by definition $C_0 = 2\, F_d / (\rho_W\, V^2 A)$ with F_d being the drag force. C_a is a dimensionless quantity in the range between 5 and 15 to quantize the pressure drop between the air inside the cavity and the water outside.

By assuming that the drag coefficient $C_d(V_r)$ is velocity-dependent, the time-dependent velocity $V_r(t)$ of the projectile after having penetrated the front plate reads:

$$V_r(t) = \sqrt{\sigma_0}\, V_{r0} \tan\left(\arctan \frac{1}{\sqrt{\sigma_0}} - k \sqrt{\sigma_0}\, V_{r0}\, t\right) \qquad (2)$$

and $k = \pi\, \rho_w \frac{1}{4} D^2\, C_0 / \left(2 m_p\right)$. It must be mentioned that equation (2) is developed in a scenario without a tank/plate i.e. the projectile impacts a plane water surface at rest.

5 Results

This paper presents results that focus on comparing numerical simulations with experimental data regarding changes in cavity size, trajectory and velocity decay of the projectile.

Fig.8: compares the measured maximum cavity diameters from the reference experiment with those obtained from the simulations as a function of time. The results from both LS-DYNA and AUTODYN-3D

are generally similar, although the simulated cavity diameters are consistently smaller than those observed in the experiment. The LS-DYNA simulation extends further into the cavity oscillation phase, demonstrating pulsations of the cavity at around 14,000 µs. As indicated in the plot, this pulsation occurs earlier than in the experiment, where the maximum cavity diameter begins to decrease at this time point. This observation suggests that while all phases of the HRAM effect are qualitatively simulated, the cavity sizes produced in the AUTODYN-3D simulations (using parameters from the AUTODYN-3D material library) and in the LS-DYNA simulations (based on [5]) exhibit significant deviations from those observed in the experiments. Therefore, further improvements to the material models used in these simulations are necessary for future work.

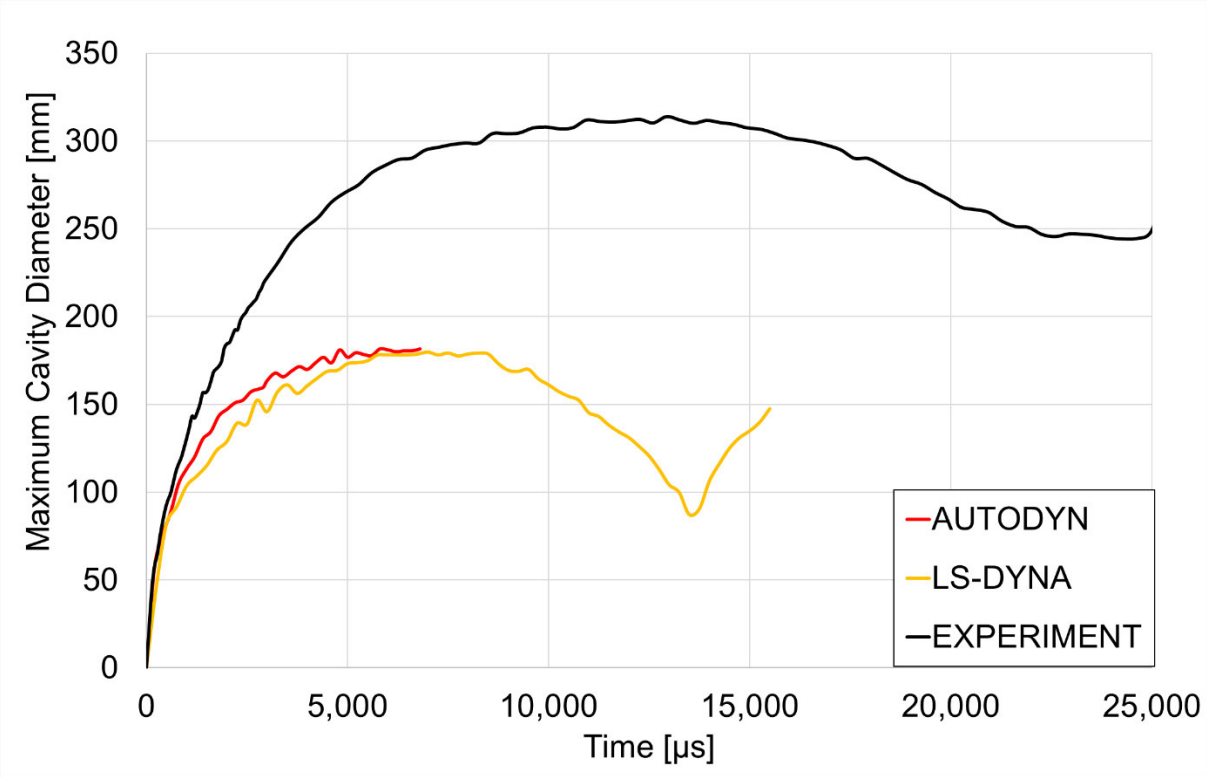

Fig.8: Maximum cavity diameter vs. time.

Fig.9: presents a comparison between the measured (grey dots) and computed y-locations versus time for the projectile's head. The dark blue and light blue curves represent the results of the analytical model from Guo et al. [13] for two impact velocities: V_0 = 645 m/s and V_{ro} = 536 m/s (the reduced velocity after impact with the front plate) respectively. The black curve is a fourth-order polynomial fit of the measured y-locations from the experiment. The red and orange curves correspond to the simulation results from AUTODYN-3D and LS-DYNA, respectively.

For the first 1,000 µs, the measured data, the simulations and analytical model curves align closely. However, as time progresses, discrepancies arise, indicating that the projectile experiences greater deceleration in the simulations than observed in the experiment under the chosen settings. The light blue curve, which approaches the black curve from the experiment, suggests that the reduced velocity resulting from the impact with the entry plate, when considered as the initial impact velocity with water, yields relatively accurate results and is similarly close to the measured data as the AUTODYN-3D simulation.

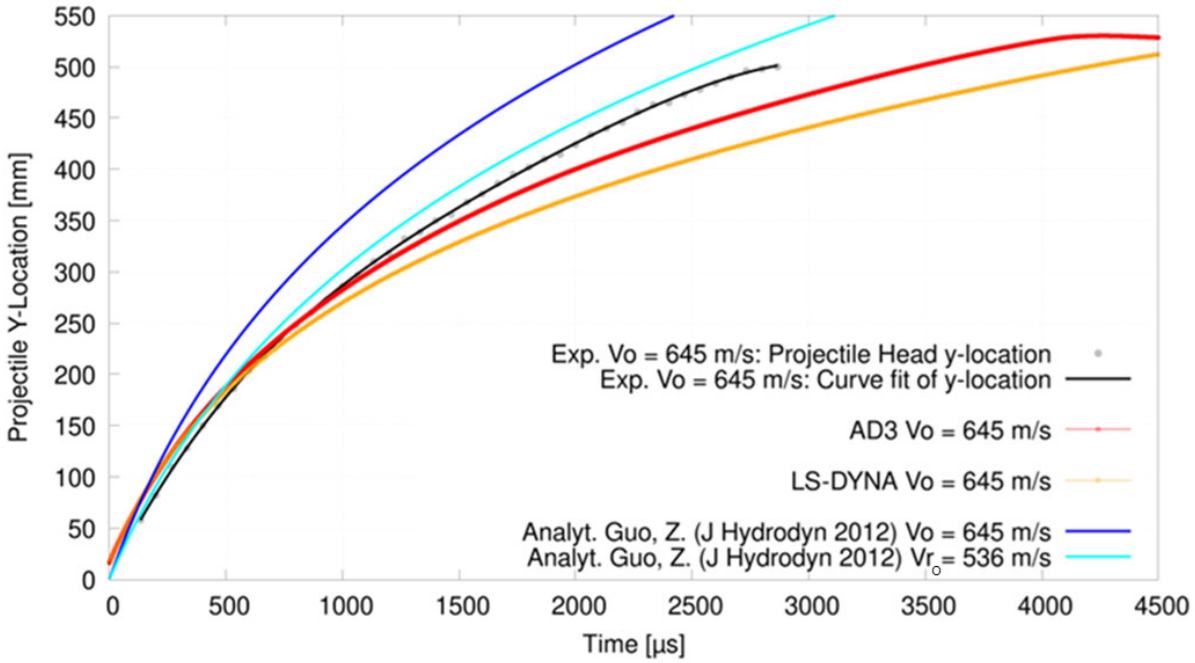

Fig.9: Projectile's y-location (shot direction) vs. time.

Fig.10: presents the corresponding diagram for the y-velocities. All curves exhibit a close overlap in terms of velocity decay, with only minor differences. The black curve, representing the experimental data, is the time derivative of the black curve shown in Fig.9:.

The region where a sudden reduction in velocity occurs in the experimental (black), LS-DYNA (orange), and AUTODYN-3D (red) curves indicates the time when the projectile reaches the end plate. As observed in the plots, these events occur at different times: approximately after 2800 µs in the experiment, around 4000 µs in AUTODYN-3D, and approximately 5100 µs in LS-DYNA. The light blue analytical curve closely aligns with the experimental curve regarding the projectile's velocity reduction. However, due to the assumption of no plates in the analytical model, the impact point with the end plate is not represented in the analytical curves.

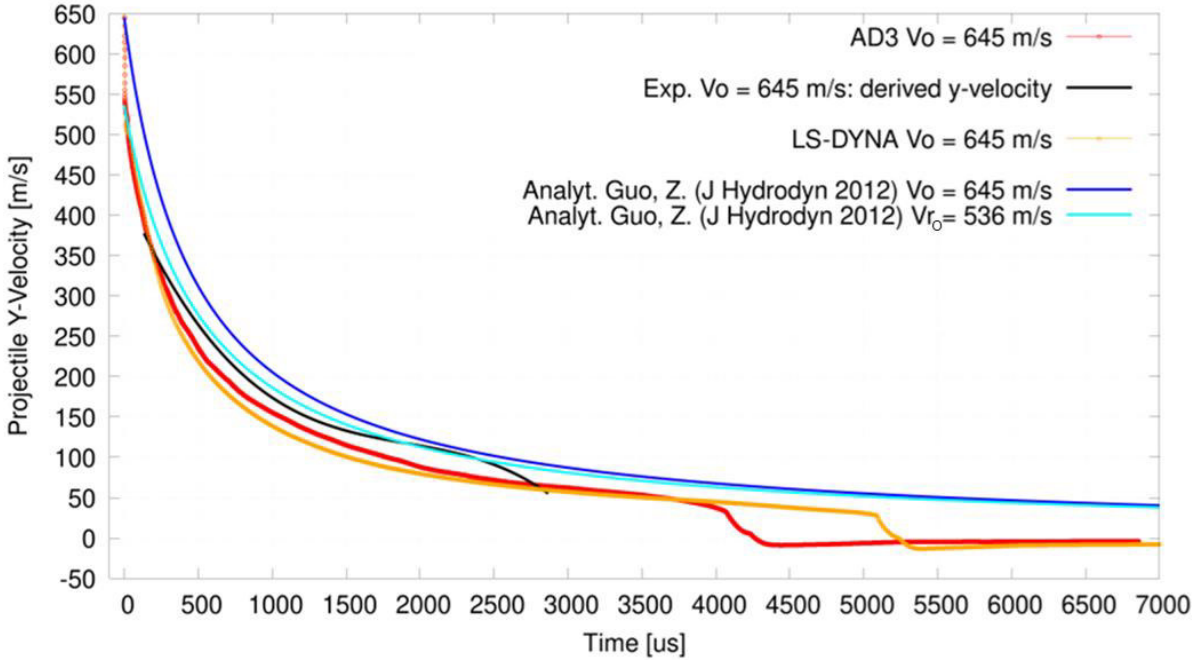

Fig.10: Projectile's y-velocity (shot direction) vs. time.

Fig.11: illustrates the projectile's trajectory in water until it impacts the rear plate of the tank. It is important to note that only the head of the projectile was visible in the high-speed camera images; therefore, the plotted trajectory represents the head position (grey dots and black curve which is the spline fit of the dots), which is relatively unstable compared to the trajectory of the center of gravity shown in the simulations.

Up to the midpoint of the tank at y = 250 mm, the red and orange curves from AUTODYN-3D and LS-DYNA coincide. Beyond this point, the projectile in AUTODYN-3D travels in the negative z-direction (i.e., towards the bottom of the tank), which is consistent with the experimental observations represented by the black curve. In contrast, the projectile in LS-DYNA moves in the positive z-direction.

This comparison is specifically intended to highlight the differences induced by the FSI settings in both hydrocodes. Based on the numerical setup, it is anticipated that the rigid projectile would travel in a straight line along the shot axis (z=0) in both simulations until it impacts the rear plate. However, this expectation is not met, as evidenced by the trajectories represented by the red and orange curves. Notably, there is a deviation of approximately z = -6 mm in the AUTODYN-3D simulation and around z = 2 mm in the LS-DYNA simulation. These deviations correspond to a small percentage range of approximately 0.46% to 1.4% relative to the tank height.

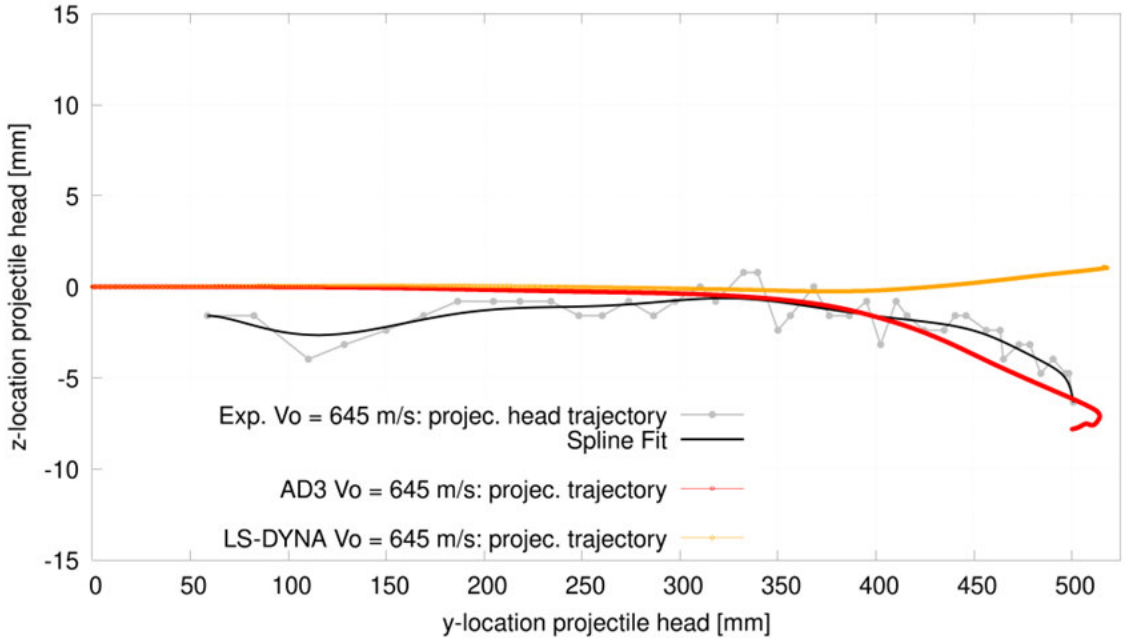

Fig.11: Projectile trajectory in y-z plane until the projectile rebounds at the tank's rear plate.

6 Summary

In this paper, the primary focus was to evaluate the capabilities of the hydrocodes LS-DYNA and AUTODYN-3D in reproducing projectile velocity decay and the evolution of the cavity size during the occurrence of the Hydrodynamic RAM (HRAM) effect, and to compare these results against experimental data and analytical methods.

The experimental setup involved a cylindrical aluminum projectile impacting a cuboidal tank at a velocity of 645 m/s, allowing for the observation of cavity dynamics and projectile behavior. High-speed imaging captured the evolution of the cavity, providing insights into the pulsations and the deceleration of the projectile.

Numerical simulations using LS-DYNA and AUTODYN-3D were conducted to replicate the experimental conditions. While both models qualitatively captured the HRAM effect, discrepancies were noted in the predicted cavity sizes as well as in the timing of cavity pulsations. In the future, a parameter optimization study for these models could be carried out to further improve the quality of the results.

The simulations effectively capture the projectile's deceleration, though not with perfect accuracy. Their performance is comparable to that of a simplified analytical model, exhibiting a similar order of quality.

In the LS-DYNA S-ALE methodology, the fluid-structure interaction (FSI) behaviour is influenced by the penalty factor and the size of the Euler cells. The LS-DYNA simulation, utilizing a tank modelled with shell elements, can qualitatively simulate all phases of the hydrodynamic RAM effect. This shows that for the HRAM case, shell elements could be implemented instead of solid elements to achieve good results while saving on computational cost.

7 Literature

[1] S. Heimbs, "Computational methods for bird strike simulations: A review," *Compos Struct,* Vols. 23-24, pp. 2093-2112, 2011.

[2] M. May and T. Strohbach, "A review on collisions between drones and aerostructures – Experimental studies, numerical simulation, and regulation," *Defence Technology,* 2025.

[3] M. May, S. Arnold-Keifer, V. Landersheim, D. Laveuve, C. Contell Asins and M. Imbert, "Bird strike resistance of a CFRP morphing leading edge," *Composites Part C,* vol. 4, p. ID 100115, 2021.

[4] G. Heilig and M. May, "The hydrodynamic RAM effect: Review of historic experiments, model developments and simulation," *Defence Technology,* vol. 44, pp. 150-178, February 2025.

[5] D. Varas, J. Lopez-Puente and R. Zaera, "Experimental analysis of fluid-filled alluminium tubes subjected to high-velocity impact," *Int. J. Impact Eng.,* vol. 36, no. 1, pp. 81-91, January 2009.

[6] A. Chen, X. Li, L. Zhou and Y. Ji, "Study of liquid spurt caused by hydrodynamic ram in liquid-filled container," *Int. J. of Impact Eng.,* vol. 144, October 2020.

[7] H. Chen, „*ALE_STRUCTURED_FSI The New S-ALE FSI Solver," [Online]. Available: https://www.dynalook.com/conferences/16th-international-ls-dyna-conference/fsi-ale-computing-technology-t8-1/t8-1-b-fsi-ale-081.pdf. [Accessed 25 June 2023].

[8] G. Heilig und M. May, „Comparison of Experimental, Numerical and Analytical approaches to HRAM events," in *AIAA 2023*, Washington, 2023.

[9] "Aluminum F39 / AW2017A parameters," [Online]. Available: https://www.gemmel-metalle.de/downloads/Legierungsbeschreibung_AlCuMg1_F39.pdf. [Accessed 5 July 2023].

[10] „Plexiglas parameters from Matweb Datasheet: Röhm Plexiglas® 100 Resist® Extruded Acrylic,"[Online].Available: https://www.matweb.com/search/datasheet.aspx?matguid=a8f971405b7c4303ad4b6469fdaf3b01&ckck=1. [Accessed 5 July 2023].

[11] J. Zhang, T. Jin, Z. Wang und L. Zhao, „Experimental investigation on yield behavior of PMMA under combined shear–compression loading," *Results in physics, 6, 265-269.,* 2016.

[12] „LS-Dyna R13 Manuals (Vol II for Material and Equation of State cards)," [Online]. Available: https://www.dynasupport.com/manuals/ls-dyna-manuals. [Accessed 25 June 2023].

[13] Z. Guo, W. Zhang and C. Wang, "Experimental and Theoretical Study on the High-Speed Horizontal Water Entry Behaviors of Cylindrical Projectiles.," *Journal of Hydrodynamics, Ser. B,* vol. 24, no. 2, pp. 217-225, 2012.

[14] P. Disimile and N. Toy, "Liquid spurt caused by hydrodynamic ram," *Int. J. of Impact Engineering,* vol. 75, no. 1, 2015.